Nonreciprocal spin pumping damping in asymmetric magnetic trilayers

Yevgen Pogoryelov, Manuel Pereiro, Somnath Jana, Ankit Kumar, Serkan Akansel, Mojtaba Ranjbar, Danny Thonig, Daniel Primetzhofer, Peter Svedlindh, Johan Åkerman, Olle Eriksson, Olof Karis, and Darío A. Arena

Phys. Rev. B **101**, 054401 — Published 3 February 2020

DOI: 10.1103/PhysRevB.101.054401

Non-Reciprocal Spin Pumping Damping in Asymmetric Magnetic Trilayers

Yevgen Pogoryelov,[1] Manuel Pereiro,[1] Somnath Jana,[1] Ankit Kumar,[2] Serkan Akansel,[2] Mojtaba Ranjbar,[3] Danny Thonig,[4] Daniel Primetzhofer,[1] Peter Svedlindh,[2] Johan Åkerman,[3,5] Olle Eriksson,[1,4] Olof Karis,[1] and Darío A. Arena[6,*]

[1] *Department of Physics and Astronomy, Uppsala University, 751 21 Uppsala, Sweden*
[2] *Department of Engineering Sciences, Uppsala University, 751 21 Uppsala, Sweden*
[3] *Department of Physics, University of Gothenburg, 412 96 Gothenburg, Sweden*
[4] *School of Science and Technology, Örebro University, 701 82 Örebro, Sweden*
[5] *Materials and Nanophysics, School of ICT, KTH Royal Institute of Technology, 164 00 Kista, Sweden*
[6] *Department of Physics, University of South Florida, Tampa, Florida 33620, USA*

In magnetic trilayer systems, spin pumping is generally addressed as a reciprocal mechanism characterized by one unique spin mixing conductance common to both interfaces. However, this assumption is questionable in cases where different types of interfaces are present. Here, we present a general theory for analyzing spin pumping in cases with more than one unique interface and where the magnetic coupling is allowed to be non-collinear. The theory is applied to analyze layer-resolved ferromagnetic resonance experiments on the trilayer system $Ni_{80}Fe_{20}$/Ru/$Fe_{49}Co_{49}V_2$ where the Ru spacer thickness is varied to tune the indirect exchange coupling. It is demonstrated that the equation of motion of macro spins driven by spin-pumping need to be modified in case of non-collinear coupling. Our analysis also shows that the spin pumping in trilayer systems with dissimilar magnetic layers in general is non-reciprocal.

Spin transport in thin film heterostructures can generate a rich spectrum of physical effects[1–9] and has great potential for realizing new spintronic functionality[10,11]. Pure spin currents, which can modify the dynamics of magnetic multilayers, can be generated in metallic ferromagnetic (FM) / non-magnetic (NM) heterostructures via the spin pumping process[12]. Precessing spins in the FM generate a spin current that can diffuse away from the FM / NM interface and into the NM layer. Propagation of spin currents in the NM can lead to spin accumulation in the NM[13], spin to charge conversion in a NM layer[14], increased Gilbert-like damping[15], and non-local perturbation of a second FM layer[16].

The efficiency of the spin pumping process across a FM / NM interface is typically parameterized by the spin mixing conductance $g^{\uparrow\downarrow}$ which relates the additional damping from spin pumping to the film thickness and intrinsic properties[12,17]. In magnetic trilayer structures (FM1 / NM / FM2), spin pumping is often treated as a reciprocal process (FM1 $\overset{\text{SP}}{\Longleftrightarrow}$ FM2), characterized by a single $g^{\uparrow\downarrow}$ common to both interfaces; this approach works well when FM1 and FM2 are the same material that generates an equivalent FM / NM interface[18,19]. Many spintronic devices rely on layered magnetic structures where FM1 and FM2 are different materials[20–25], with different interfaces on each side of the spacer layer. In several cases these systems have more complex interlayer exchange, such as biquadratic exchange, combined with non-collinear magnetic configurations. This calls for an analytical framework to analyse magnetisation dynamics of such systems, where such complexities are explicitly considered. We provide such an theoretical model in this article, together with experimental data.

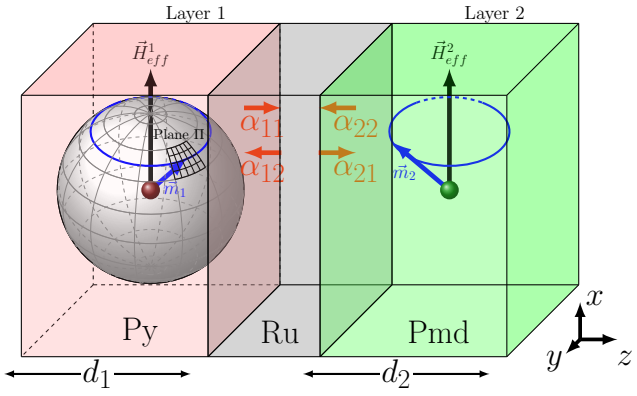

FIG. 1. (Color online) Trilayer system composed of Permalloy (1) and Permendur (2) layers separated by a Ruthenium spacer. The coordinate system is shown on the bottom right. The blue arrow represents the precession of the spin in the $\hat{\boldsymbol{y}} - \hat{\boldsymbol{z}}$ plane and the black arrow indicates the direction of the external magnetic field. The sphere represents the locus of constant magnetization length while Π stands for the plane tangential to the surface of the sphere. The red-yellow arrows indicate the local (α_{ii}) and inter-layer (α_{ij}) spin pumping damping due to the currents flowing in and out of the layers. The magnetic layer's thickness is represented by d_1 and d_2.

The model proposed accounts for FM1 and FM2 layers with different intrinsic parameters. Two key features of the treatment are (a) the separation of the spin-mixing conductance into distinct contributions for the two dissimilar interfaces, and (b) a self-consistent macrospin framework for non-colinear magnetizations. We apply this theory to analyze layer-resolved ferromagnetic resonance (FMR) experiments measured with X-ray detected FMR (X-FMR) from magnetic trilayer samples

* Corresponding author: darena@usf.edu

where the NM spacer thickness is varied to tune the indirect exchange coupling. The analysis demonstrates that the spin pumping damping from FM1 into FM2 is *non-reciprocal* with the spin pumping damping in the reverse direction. The non-reciprocity is significant, which may enable new spintronics technologies.

We consider a trilayer system involving Permalloy (Py - $Ni_{80}Fe_{20}$), Ru and Permendur (Pmd - $Fe_{49}Co_{49}V_2$). In the Py/Ru/Pmd system, the Py and Pmd layers provide large magnetic moments, while Ru is the NM spacer. In the following, the first magnetic layer (Py) is labeled by 1 and the second magnetic layer by 2 (Pmd), as shown in Fig. 1. We assume that each layer can be represented by a single $\boldsymbol{m}_i$ and $\boldsymbol{m}_j$ (macrospin approximation), where $i, j = 1, 2$.

The equation of motion of the macrospins can be recast as:

$$\begin{aligned}\frac{\partial \boldsymbol{m}_i}{\partial t} =& -\gamma \boldsymbol{m}_i \times \boldsymbol{H}^i_{\text{eff}} + (\alpha^0_i + \alpha^{sp}_{ii})\boldsymbol{m}_i \times \frac{\partial \boldsymbol{m}_i}{\partial t} \\ &- \frac{\alpha^{sp}_{ij}}{|\boldsymbol{m}_i|^2}\boldsymbol{m}_i \times \left(\boldsymbol{m}_j \times \frac{\partial \boldsymbol{m}_j}{\partial t}\right) \times \boldsymbol{m}_i \end{aligned} \quad (1)$$

where $\gamma \approx 3.5 \cdot 10^{-5}\,(\text{GHz}\cdot\text{m})/\text{A}$ is the gyromagnetic ratio. Both macrospins ($\boldsymbol{m}_i$, $i = 1, 2$) precess around their effective fields $\boldsymbol{H}^i_{\text{eff}} = -\partial\mathcal{H}/\partial\boldsymbol{m}_i$, where $\mathcal{H}$ is the spin-Hamiltonian. The non-local, inter-layer damping, α^{sp}_{ij}, accounts for spin-pumping contributions into layer i from layer j, while the local damping, α^{sp}_{ii}, parameterizes spin-pumping out of layer i. The influence of the spin-pumping damping (α^{sp}_{ij}) on the model is discussed in the Appendix A. The intrinsic damping of layer i is given by α^0_i. The last term is of a form previously not discussed, and represents the influence of non-local dynamic spin-pumping of a non-collinear magnetic arrangement between two ferromagnetic layers of a trilayer system. This term describes a projection of the vector $\boldsymbol{m}_j \times \frac{\partial \boldsymbol{m}_j}{\partial t}$ from layer j over the plane Π tangential to the sphere circumscribed by the macrospin i, as shown in Fig. 1. The last term of Eq. (1) fulfills the requirement that the rate of change of magnetization ($\frac{\partial \boldsymbol{m}_i}{\partial t}$) is perpendicular to the magnetization ($\boldsymbol{m}_i$) at all times ($\boldsymbol{m}_i \cdot \frac{\partial \boldsymbol{m}_i}{\partial t}$=0).

The coupled trilayer system in the coordinate system indicated in Fig. 1 is described by the following Hamiltonian $\mathcal{H}$:

$$\begin{aligned}\mathcal{H} =& -\frac{A_{ex}}{\mu_0 d_i}\frac{\boldsymbol{m}_i \cdot \boldsymbol{m}_j}{|\boldsymbol{m}_i||\boldsymbol{m}_j|} - \frac{B_{ex}}{\mu_0 d_i}\frac{(\boldsymbol{m}_i \cdot \boldsymbol{m}_j)^2}{|\boldsymbol{m}_i|^2|\boldsymbol{m}_j|^2} + \frac{1}{2}\bar{\bar{N}}_i \boldsymbol{m}_i^2 \\ &- H_0 \widehat{\boldsymbol{x}} \cdot \boldsymbol{m}_i + \frac{1}{2}\delta_i \widehat{\boldsymbol{x}} \cdot \boldsymbol{m}_i - h\widehat{\boldsymbol{y}} \cdot \boldsymbol{m}_i \\ &+ \frac{K^u_{1i}}{\mu_0|\boldsymbol{m}_i|^2}(\boldsymbol{m}_i \cdot \widehat{\boldsymbol{e}}_u)^2 + \frac{K^c_{1i}}{\mu_0|\boldsymbol{m}_i|^4}\Big[(\boldsymbol{m}_i \cdot \widehat{\boldsymbol{x}})^2(\boldsymbol{m}_i \cdot \widehat{\boldsymbol{y}})^2 \\ &+ (\boldsymbol{m}_i \cdot \widehat{\boldsymbol{y}})^2(\boldsymbol{m}_i \cdot \widehat{\boldsymbol{z}})^2 + (\boldsymbol{m}_i \cdot \widehat{\boldsymbol{z}})^2(\boldsymbol{m}_i \cdot \widehat{\boldsymbol{x}})^2\Big] \end{aligned} \quad (2)$$

where the first (A_{ex}) and second (B_{ex}) term represent the bilinear- and biquadratic exchange energy, respectively. The parameter d_i indicates the thickness of the ferromagnetic layer while $\mu_0 \approx 4\pi \cdot 10^{-7} J/(m \cdot A^2)$ is the vacuum permeability. The next term is the demagnetization energy. In a thin film with $x, y \gg z$ and with the magnetization in-plane (x-y plane), the demagnetization tensor $\bar{\bar{N}}_i$ is almost zero and will not be considered hereafter. The fourth term (H_0) represents the energy of a static external magnetic field along the $\widehat{\boldsymbol{x}}$ direction while the following term is the magnetic dipolar field where δ_i is a term that depends on the structural parameters of the layer as shown in Ref. [26]. We consider here only the influence of the field along the $\widehat{\boldsymbol{x}}$ direction since the dipolar field at a distant point (0,0,z) has only x-component for the field. The next term is the microwave field $h = \tilde{h}e^{-i\omega t}$ oscillating at a frequency ω along the $\widehat{\boldsymbol{y}}$ direction in the experimental setup. Finally, the last two terms represent the uniaxial (with the easy axis $\boldsymbol{e}_u$) and cubic magnetocrystalline anisotropy energy, respectively.

Since the moments rotate around the external magnetic field, the condition $m^x \gg m^y, m^z$ is fulfilled; hence $\frac{dm^x_i}{dt} = 0$. Moreover, the sinusodial microwave field induces a magnetisation that conveniently can be expressed in a complex form. Thus, $m^y_i(t) = \tilde{m}^y_i \exp[i(\phi_i + \omega_i t)]$, $m^z_i(t) = \tilde{m}^z_i \exp[i(\phi'_i + \omega_i t)]$ with $\phi'_i = \phi_i + \pi/2$ and $\omega = \omega_i$. The phase ϕ_i at time t=0 of layer i is a function of the external magnetic field and is measured by X-FMR experiments (see Fig. 2d-f). Assuming that the angle of precession of the macrospin is relatively small ($m^x \gg m^y, m^z$) and also that $h \ll H_0$, it is a good approximation to linearize the equations of motion. We retain only the terms linear in h, m^y and m^z. By inserting Eq. (2) into Eq. (1) through the definition of the effective field, the linearized coupled equations of motion for both magnetic layers are given by:

$$\bar{\bar{\chi}}\begin{pmatrix}0\\ \tilde{h}\\ 0\\ \tilde{h}\end{pmatrix} = \begin{pmatrix}\tilde{m}^y_1\\ \tilde{m}^z_1\\ \tilde{m}^y_2\\ \tilde{m}^z_2\end{pmatrix} \quad (3)$$

where the elements of the magnetic susceptibility matrix, $\bar{\bar{\chi}}$ are shown in Appendix B. The dimensionless intrinsic Gilbert damping parameter is defined as $\eta^0_i = m^x_i \alpha^0_i$. The spin pumping damping parameter out of layer i is $\eta^{sp}_{ii} = m^x_i \alpha^{sp}_{ii}$, while the dimensionless spin backflow into layer i from layer j is defined as $\eta^{sp}_{ij} = m^x_j \alpha^{sp}_{ij}$. The amplitude of the macrospin precession shown in Fig. 2 (a) – (c) is calculated from the four-index susceptibility matrix[27] of the system, $\bar{\bar{\chi}}$, as:

$$\psi_1 = \sqrt{[\Re(\chi_{12} + \chi_{14})]^2 + [\Im(\chi_{12} + \chi_{14})]^2} \quad (4)$$

$$\psi_2 = \sqrt{[\Re(\chi_{32} + \chi_{34})]^2 + [\Im(\chi_{32} + \chi_{34})]^2}. \quad (5)$$

where ψ_1 and ψ_2 represent the amplitudes of Py and Pmd layers, respectively.

X-FMR[28–31] is the ideal technique to investigate non-reciprocal spin pumping damping. Using X-FMR it is feasible to measure the full complex susceptibility (χ' and

χ'')[32] or equivalently the amplitude and phase of oscillation resolved to individual elements and hence distinct magnetic layers[33–35]. X-FMR was used to determine the relative orientation of precessing spins in ferrimagnets[36] as well as to examine topics including spin pumping and the influence of spin currents[37–39]. For the investigation of non-reciprocal spin pumping damping, the measured response of the individual layers can be compared directly with the equation of motion [Eq. (1)] for FM1 and FM2.

We use the X-FMR technique to study a series of Py / Ru / Pmd magnetic trilayer film structures. The film samples were fabricated at room temperature using dc magnetron sputtering (base pressure of 5×10^8 Torr) with the following structure: substrate/Ta(30 Å)/Py(80 Å)/Ru(t_{Ru})/Pmd(80 Å)/Ta(30 Å). Here t_{Ru} varies between 7 – 170 Å. Single films of Pmd and Py with the same seed and cap layers were also fabricated for control measurements. The Ru spacer layer was deposited at low sputtering rate (0.4 Å/s) and low Ar gas pressure (3 mTorr) for optimal uniformity and interface smoothness. Composition and thickness of the films was verified using Rutherford Backscattering Spectrometry (RBS). Each sample was fabricated simultaneously on an oxidized Si-substrate for magnetometry and structural measurements and on a 100 nm thick Si_3N_4 membranes for X-FMR. To minimize the number of free parameters in Eq. (2), we conducted a series of static magnetometry and FMR measurements on the samples. In the X-FMR studies, the Ni in Py and Co in Pmd provide the elemental contrast to resolve the dynamics in the individual FM layers while Ru produces a strong interlayer exchange coupling that can be tuned from favoring parallel or anti-parallel ground state coupling as a function of the NM spacer thickness[40].

In X-FMR we perform time delay scans (equivalent to varying the phase between the sinusoidal RF excitation at 3.96 GHz and the X-ray bunches) with the photon energy tuned to the Ni or Co L_3 edge. The inset to Fig. 2(b) presents a subset of these delay scans; additional details on X-FMR are presented in Appendix C and in Ref. [32]. The amplitude and phase of the sinusoidal waveforms are extracted and plotted as discrete points in Fig. 2 (a) – (f). Also shown as insets to Fig 2-(d),-(e) and -(f) are normalized magnetization curves for the $t_{Ru} = 170$ Å, 12 Å, and 7 Å samples, showing the magnetic coupling is very weak (170 Å-Fig. 2d), ferromagnetic (12 Å–Fig. 2e), and biquadratic (7 Å-Fig. 2f).

The $t_{Ru} = 170$ Å sample does not exhibit any bilinear or biquadratic interlayer exchange coupling and the amplitude data in Fig. 2 (a) reveal two resonances at ∼27 mT and at ∼9 mT. The coupled nature of the dynamics of the FM layers precludes assignment of the combined resonance to a single layer and we refer to these as a low field and high field resonance (LFR or HFR). The other samples also present a LFR and HFR. At either resonant field, a particular FM layer does not respond independently; the other layer also exhibits a distinct, albeit weaker, response. This is clear *e.g.* from Fig. 2 (a), where the Py and Pmd layer has a maximum at the HFR and LFR, respectively. However, each layer has a second smaller peak in the amplitude that coincides with the resonance field of the other magnetic layer. This produces a non-trivial behaviour of the amplitudes, originating from the coupling between the layers, and we observe a similar effect for all samples of this investigation.

The phase data also reveal a complex response of the oscillation phase as the magnetic field is swept through the resonance. For non-interacting layers, the phase of FM1 would change by 180° when passing through the resonant field while the other layer would remain essentially unchanged. For coupled magnetic layers the phases of the dynamic response would change according to Eq. (3). In the sample with the weakest coupling between Py and Pmd ($t_{Ru} = 170$ Å, Fig. 2 (d)), the phase of the Py layer changes by ∼180° through the HFR. However, the Pmd layer undergoes approximately the same phase shift through the HFR and then experiences an additional phase shift of ∼120° through the LFR, indicating that there is sufficient coupling to cause a response distinctly different from that of non-interacting layers.

The variations in amplitude and phase are even more dramatic for the more strongly coupled samples ($t_{Ru} = 12$ Å and 7Å). In these systems, the phase of the Py layer shifts by about 180° as the field is tuned from high fields down through the HFR; the Pmd phase initially follows the increase in phase, but once the HFR is passed it falls off again. The effect is particularly pronounced in the FM-coupled $t_{Ru} = 12$ Å sample, where the two phases are essentially equal from high field down through the HFR at ∼16 mT. As the field is reduced towards the LFR, the Pmd phase rises sharply to approach a value that is ∼120° lower than that of the Py layer. For the $t_{Ru} = 7$ Å sample with biquadratic coupling, the phases of the two layers are distinctly different for all field strengths. This suggests, somewhat surprisingly, that the system with the closest distance between the Py and Pmd layers, has the largest degree of independence in the magnetic response of both Py and Pmd.

We begin our analysis with the phase data in Fig. 2 (d), (e) and (f). We fit the experimental phase data with a high order B-spline[41] and use these interpolated values for the phase, together with the parameters for magnetization, anisotropy and interlayer exchange, to calculate the amplitude response based on Eqs. (4)-(5). The results are presented as the solid lines in Fig. 2 (a), (b), and (c). Apart from the phase data, all sample parameters used in the amplitude calculations (*i.e.* magnetization, anisotropy, layer thickness, exchange parameters, *etc.*) were obtained from independent magnetometry and conventional ferromagnetic resonance measurements (see Appendix D for details).

Generally, the theoretical model is in good agreement with the data in Fig. 2. The model captures the essential features of the Py and Pmd layers, across both the LFR and HFR; peak positions and amplitudes are well-reproduced for the main resonance and also the weaker

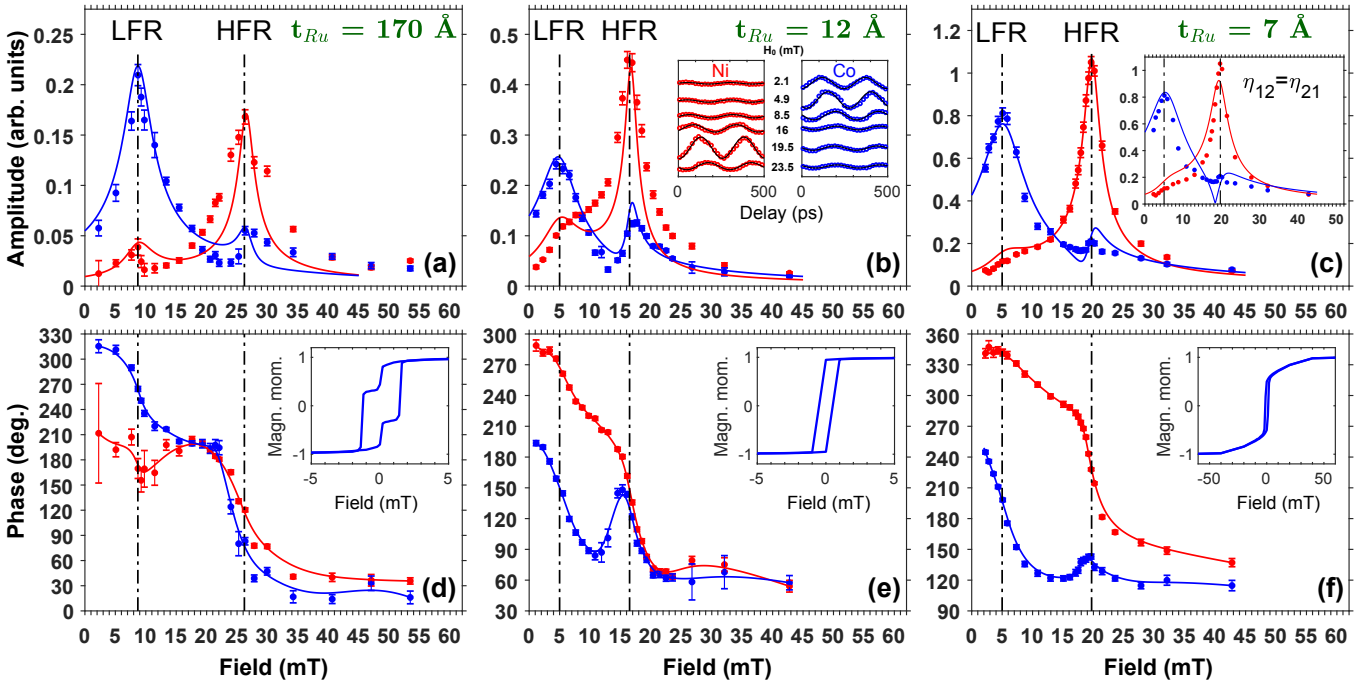

FIG. 2. (color online) Non-reciprocal spin pumping damping theory and X-FMR measurements. Measured X-FMR amplitude and phase data (discrete points) acquired at an excitation frequency of 3.96 GHz are shown as function of applied field for three different Ru spacer layer thicknesses: 170 Å(a,d) 12 Å(b,e) and 7 Å(c,f). Solid lines in the graphs showing the phase are high order B-splines while the solid lines for the amplitude response are model calculations based on Eq. (1). The Pmd layer response is shown in blue while the Py is in red. The inset to (b) presents typical X-FMR delay scans for the Co and Ni edges acquired at different static bias fields. Inset in (c) shows model calculations for the t_{Ru} 7 Å sample with symmetric spin pumping damping ($\eta_{12} = \eta_{21}$= 0.54). Insets in (d,e,f) present static magnetometry data, showing independent switching / no coupling (170 Å -(d)), ferromagnetic coupling (12 Å-(e)), and biquadratic interaction (7 Å-(f)).

response connected to the second layer. For example, in the coupled tri-layer sample with shortest interlayer distance (Fig. 2 (c), t_{Ru} = 7 Å), the model reproduces the increased amplitude in the response of the Pmd layer at the resonant field of the Py layer. For the ferromagnetically coupled sample (Fig. 2 (b), t_{Ru} = 12 Å), the model accurately produces a reduced amplitude of the Pmd response at 5 mT in comparison with the main Py resonance at 16 mT, in agreement with our experimental observations. The sample with the thickest Ru spacer (Fig. 2 (a), t_{Ru} = 170 Å), where interlayer exchange and dipolar coupling effects are negligible, is particularly interesting. For completely decoupled layers, we would expect that the amplitude of the two resonances can be described by smooth, symmetric Lorentzian functions. However, the experimental data show an increase of the Pmd (Py) amplitude at the resonant field of the Py (Pmd) layer, and a deviation from Lorentzian shape, an effect that is clearly reproduced by the theory.

By using the measured phase response, along with the independently derived material parameters, our model provides estimates of the precessional damping and the contributions from spin pumping (see Table I). $\Re\ (g_i^{\uparrow\downarrow})$ (the real part of the spin mixing conductance of layer i) is related to the dimensionless spin pumping parameter η_{ij} as[42]:

$$\Re(g_i^{\uparrow\downarrow}) = \frac{8\pi m_j^x d_j \eta_{ji}}{g_j \mu_B}, \text{ where } i \neq j. \qquad (6)$$

Here, g_j is the spectroscopic g-factor and μ_B is the Bohr magneton. The contributions of the two interfaces (Py / Ru or Ru / Pmd) to the spin mixing conductance are not reciprocal. For all the samples studied, we observe that the real part of the spin-mixing conductance from the Py layer, that influences the Pmd layer, is clearly bigger than the reversed spin-mixing conductance. The latter is close to values reported in the literature [42]. A symmetric spin pumping damping model reproduces the data poorly, as can be seen in the inset to Fig. 2-c, which assumes $\eta_{12} = \eta_{21} = 0.54$. Apart from an overall poor description of the shape of the X-FMR data, such a model overestimates the magnitude of the Pmd (Py) response at most fields.

In the standard picture of spin pumping, a magnetic layer excited into precession drives a diffusive spin current in the direction transverse to the FM1 / NM interface. The spin current incident upon the NM layer leads to spin accumulation in the NM near the interface and generates a flow of spin current back to the FM1.

The spin mixing conductance parameterizes the balance of the initial spin current (FM1 → NM) and the backflow into the magnetic layer. For NM layers that are thin compared to the spin diffusion length in this layer (∼150Å in Ru[43]) the spin current driven transports angular momentum across the NM / FM2 interface (with its own characteristic spin mixing conductance) and thereby influencing the dynamics of FM2. The two spin mixing conductances are often assumed to be equivalent[42]. However, the multilayer spin pumping theory presented above together with the X-FMR data clearly indicate that spin pumping damping is non-reciprocal (*i.e.* dependent on direction of the spin current normal to the interface) in systems with nonequivalent interfaces[44–46]. The asymmetry of the spin-mixing conductance, albeit little discussed, is physically motivated, as it is proportional to the self-energy and the electronic structure of the respective magnetic layer[47]. There is no reason why this self-energy should be the same for Py and Pmd. In terms of symmetry, the non-reciprocity of the spin pumping damping could be explained by breaking of the space inversion symmetry in the neighborhood of the interfaces induced by having two dissimilar ferromagnetic layers, as it was shown in Ref. [48] for the non-reciprocal magnon transport in synthetic magnets.

Interface spin transport governs a variety of phenomena such as spin injection, the generation of pure spin currents, and the determination of spin Hall angles[3,49–51]. Spin pumping presents another method for manipulating magnetization across an interface, allowing for nonlocal effects. Spin pumping damping in magnetic trilayers has been examined previously in configurations with both parallel alignment and anti-parallel moments canted in the direction of an external field[52,53]. Our analysis extends spin pumping theory towards more general magnetic multilayer structures, which may have non-collinear or biquadratic interlayer exchange, different layer anisotropies and distinctly different spin-mixing conductances. These effects will influence the dynamics of individual layers; however, when these issues are assessed independently, the asymmetry of the spin pumping damping is revealed. Also, the description of magnetisation dynamics, in Eq. (1), is novel, since it allows for spin-pumping in non-collinear systems. In this work, we report for the first time non-reciprocal spin pumping damping in magnetic trilayers with dissimilar interfaces, and our findings may open new possibilities in spintronics technology. Earlier first principles calculations of spin pumping indicate that band matching across the interface (the matching of states in the NM with spin-resolved propagating states in the FM layer), greatly affects spin transmission and reflection across the interface[44,45]. Our analysis supports this viewpoint and shows that X-FMR can uniquely reveal differences in spin pumping damping. Finally, we note that additional contributions to spin pumping damping, such as spin-orbit coupling at the Ru / FM interfaces and spin current backflow variations for thick NM spacer layers, may affect the mutual spin dynamics in the FM layers. These contributions are being investigated with on-going first principles calculations of the FM / NM interfaces, spin transport theory, and additional analytical modeling.

TABLE I. Estimated spin pumping induced damping parameters and real part of the spin mixing conductance in cm^{-2} for samples with t_{Ru} = 7 Å, 12 Å and 170 Å.

t_{Ru} Å	η_{11}^{sp} 10^{-4}	η_{22}^{sp} 10^{-3}	η_{12}^{sp}	η_{21}^{sp}	$\Re(g_1^{\uparrow\downarrow})$ 10^{15}	$\Re(g_2^{\uparrow\downarrow})$ 10^{15}
7	3	1.6	0.47	0.61	11.75	3.64
12	3	1.0	0.69	0.45	8.65	5.33
170	3	9.2	0.30	0.40	7.76	2.30

ACKNOWLEDGMENTS

The authors gratefully acknowledge the support of the Knut and Alice Wallenberg foundation, the Foundation for Strategic Research, eSSEENCE, StandUPP, the Swedish Energy Agency, the Swedish research council (VR) under contracts 2016-04524, and 2013-08316. D.A.A. acknowledges partial support through a University of South Florida Nexus Initiative (UNI) Award. This research used resources of the Advanced Photon Source, operated for the U.S Department of Energy Office of Science by Argonne National Laboratory under Contract No. DE-AC02-06CH11357.

Appendix A: Influence of spin-pumping damping

In Figs. (3-4), we show the influence of the variation of the spin-pumping damping on the amplitude of the resonant response, for the particular case of the sample with Ru thickness of 7 Å. In general, a small variation of the spin-pumping damping produces a significant variation of the amplitude particularly around the resonance field. Since η_{21} determines the spin-pumping in Pmd layer produced by Py layer, the small resonant peak (or secondary peak) at around 20 mT varies with η_{21} (see Fig. (3), dashed red and dotted black lines) while the small resonant peak at around 5 mT is unchanged. Notice also that if η_{21} decreases, the secondary resonant peak also decreases and vice-versa. The physical interpretation is as follows: By decreasing the spin-pumping damping, the Pmd layer experiences a smaller influence of the magnetization precession in Py layer. The same line of reasoning is applied to the spin-pumping damping η_{12} as shown in Fig. (4).

The FMR results are generally consistent with single layer damping values presented in Table I. In particular, the FMR linewidth data indicate a higher damping value for the Pmd layer in the t_{Ru} = 170 Å sample, as might be expected with a slightly rougher Ru / Pmd interface with the thicker Ru spacer.

TABLE II. Estimated exchange constants and intrinsic dampings for samples with t_{Ru} = 7 Å, 12 Å and 170 Å.

t_{Ru}	A_{ex} (J/m^2)	B_{ex} (J/m^2)	η_1	η_2
7	0	$-10.5 \cdot 10^{-5}$	0.00852	0.00426
12	$4.5 \cdot 10^{-5}$	0	0.00852	0.00442
170	0	0	0.00852	0.00640

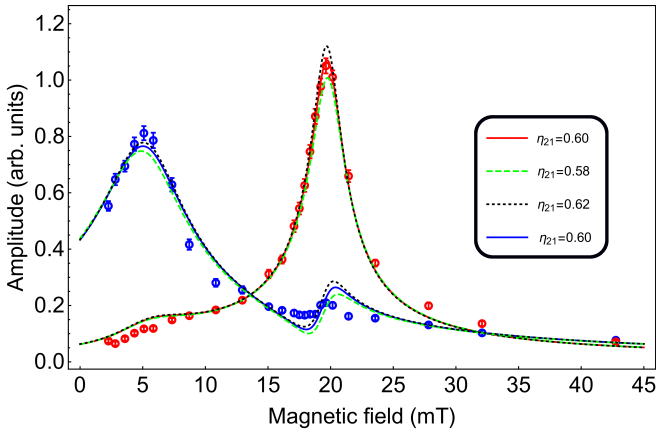

FIG. 3. (Color online) Amplitude of the resonant response for the sample with Ru thickness of 7 Å. The spin-pumping damping η_{21} has been varied while keeping constant the remaining parameters expect for the dipolar field and the scaling parameter. The spin-pumping damping η_{12} was fixed to 0.47.

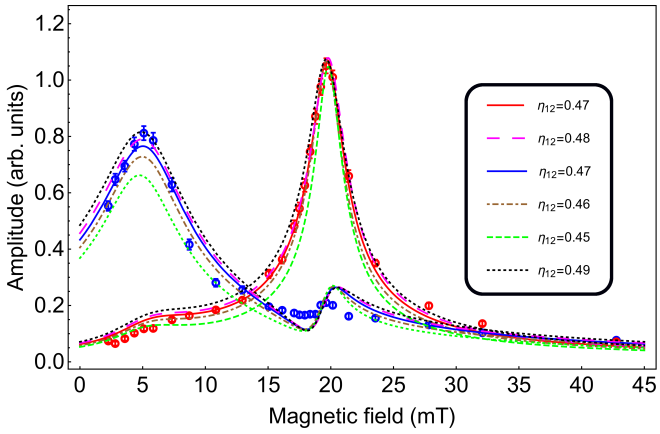

FIG. 4. (Color online) Amplitude of the resonant response for the sample with Ru thickness of 7 Å. The spin-pumping damping η_{12} has been varied while keeping constant the remaining parameters expect for the dipolar field and the scaling parameter. The spin-pumping damping η_{21} was fixed to 0.60.

Appendix B: Non-Reciprocal Spin Pumping Damping Theory

The magnetic susceptibility, which is a 4×4 matrix (according to Eq. (3) of the main part of the paper), is defined as:

$$\bar{\bar{\chi}} = \bar{\bar{\mathcal{A}}}^{-1} \tag{B1}$$

where the elements of the matrix $\bar{\bar{\mathcal{A}}}$ are:

$$a_{11} = \frac{-i\omega e^{i\phi_1}}{\gamma m_1^x},$$
$$a_{12} = \left(-\frac{A_{ex}+2B_{ex}\cos\beta}{\mu_0 d_1 {m_1^x}^2} - \frac{H_0-\delta_1}{m_1^x} - \frac{2K_{11}^c}{\mu_0 {m_1^x}^2} + \frac{2K_{11}^u}{\mu_0 {m_1^x}^2}\cos^2\theta_1 - \frac{(\eta_1^0+\eta_{11}^{sp})i\omega}{\gamma m_1^x}\right) ie^{i\phi_1},$$
$$a_{13} = 0,$$
$$a_{14} = \left(\frac{A_{ex}+2B_{ex}\cos\beta}{\mu_0 d_1 m_1^x m_2^x} + \frac{\eta_{12}^{sp} i\omega}{\gamma m_1^x}\right) ie^{i\phi_2},$$
$$a_{21} = \left(\frac{2K_{11}^u}{\mu_0 {m_1^x}^2}(1-2\cos^2\theta_1) + \frac{2K_{11}^c}{\mu_0 {m_1^x}^2} + \frac{A_{ex}+2B_{ex}\cos\beta}{\mu_0 d_1 {m_1^x}^2} + \frac{H_0-\delta_1}{m_1^x} + \frac{(\eta_1^0+\eta_{11}^{sp})i\omega}{\gamma m_1^x}\right) e^{i\phi_1},$$
$$a_{22} = \frac{\omega e^{i\phi_1}}{\gamma m_1^x},$$
$$a_{23} = \left(-\frac{A_{ex}+2B_{ex}\cos\beta}{\mu_0 d_1 m_1^x m_2^x} - \frac{\eta_{12}^{sp} i\omega}{\gamma m_1^x}\right) e^{i\phi_2},$$
$$a_{24} = 0,$$
$$a_{31} = 0,$$
$$a_{32} = \left(\frac{A_{ex}+2B_{ex}\cos\beta}{\mu_0 d_2 m_1^x m_2^x} + \frac{\eta_{21}^{sp} i\omega}{\gamma m_2^x}\right) ie^{i\phi_1},$$
$$a_{33} = \frac{-i\omega e^{i\phi_2}}{\gamma m_2^x},$$
$$a_{34} = \left(\frac{-2K_{12}^c}{\mu_0 {m_2^x}^2} - \frac{A_{ex}+2B_{ex}\cos\beta}{\mu_0 d_2 {m_2^x}^2} - \frac{H_0-\delta_2}{m_2^x} + \frac{2K_{12}^u\cos^2\theta_2}{\mu_0 {m_2^x}^2} - \frac{(\eta_2^0+\eta_{22}^{sp})i\omega}{\gamma m_2^x}\right) ie^{i\phi_2},$$
$$a_{41} = \left(-\frac{A_{ex}+2B_{ex}\cos\beta}{\mu_0 d_2 m_1^x m_2^x} - \frac{\eta_{21}^{sp} i\omega}{\gamma m_2^x}\right) e^{i\phi_1},$$
$$a_{42} = 0,$$
$$a_{43} = \left(\frac{2K_{12}^u}{\mu_0 {m_2^x}^2}(1-2\cos^2\theta_2) + \frac{2K_{12}^c}{\mu_0 {m_2^x}^2} + \frac{A_{ex}+2B_{ex}\cos\beta}{\mu_0 d_2 {m_2^x}^2} + \frac{H_0-\delta_2}{m_2^x} - \frac{(\eta_2^0+\eta_{22}^{sp})i\omega}{\gamma m_2^x}\right) e^{i\phi_2},$$
$$a_{44} = \frac{\omega e^{i\phi_2}}{\gamma m_2^x}.$$

The angle between the direction of the magnetization in Py layer with respect to the magnetization in Pmd layer is indicated here by the symbol β. By using the data collected in Tables IV-II and the measured phase shown in Fig. 2, the model described by Eq. (3) provides the spin-pumping dampings, angle β and dipolar field prefactors (δ_i). These data are collected in Tables I and III.

TABLE III. Angle between the direction of the magnetization in Py layer with respect to the magnetization in Pmd layer as well as the layer-dependent dipolar field prefactor for samples with t_{Ru} = 7 Å, 12 Å and 170 Å.

t_{Ru}	β	δ_1	δ_2
	rad	mT	mT
7	2	-117.78	111.88
12	0	-91.83	121.56
170	0	-124.02	156.29

Appendix C: X-FMR Measurements

X-ray detected ferromagnetic resonance[28–31], or X-FMR, is the ideal technique to investigate non-reciprocal spin pumping damping. X-FMR combines x-ray magnetic circular dichroism (XMCD) with FMR and an overview of the technique is presented in Fig. 5. As with measurements of element-specific hysteresis loops, tuning the x-ray energy to the absorption edge of different elements (*e.g.* the Co or Ni L_3 edges) isolates the magnetic contribution from a single layer in a multilayer magnetic structure. And by using a microwave FMR excitation that is phase-locked with the x-ray bunch clock

at a synchrotron storage ring, the full complex susceptibility (χ' and χ'')[32] or equivalently the amplitude and phase of the FMR oscillation is resolved to individual elements and hence distinct magnetic layers[33–35]. X-FMR was previously used to determine the relative orientation of precessing spins in ferrimagnets[36] as well as to examine topics including spin pumping and the influence of spin currents[37,38,55,56]. For the investigation of non-reciprocal spin pumping damping, the measured motion of the individual layers via X-FMR can then be compared directly with results that come from the equation of motion [Eq. (1)] for FM1 and FM2.

In our implementation of the technique, X-FMR is a pump-probe measurement where the pump is a sinusoidal RF signal that is phase-locked to the photon bunch repetition frequency of the synchrotron. The probe is the circularly polarized x-rays whose energy is tuned to the L_3 absorption edge of Co for sensitivity to the Pmd layer or Ni for the Py layer (see Fig. 5 (a)). The thin film sample is placed on a custom co-planar waveguide that permits transmission of the incident x-rays. The RF signal excites precession of the magnetization in the magnetic layers and the x-rays transmitted through the sample are detected with a photodiode (Fig. 5 (b)). We conducted the X-FMR measurements at beamline 4-ID-C of the Advanced Photon Source (Argonne National Lab, Argonne, IL USA). In X-FMR experiments we perform time delay scans, which are equivalent to varying the phase between the sinusoidal RF signal and the arrival of the x-ray photons. Fig. 5 (c) presents a subset of these delay scans; for further details, refer to [29]. The X-ray photon bunches with a bunch length of ∼60 ps[32] sample the projection of the magnetization along the beam propagation direction as a function of time delay or phase. The simple sinusoidal waveforms of the delay scans allow us to extract the amplitude of the precessional motion and phase relative to the microwave field of the pump. We use a fixed frequency of 3.96 GHz (the 45^{th} harmonic of the 88 MHz bunch repetition frequency of the synchrotron) and recorded the response of the Pmd and Py layers as we varied the static bias field H_B through both the high- and low-field resonances. The resulting amplitude and phase data for the three samples are shown in Fig. 2 (a) - (f) of the main text as discrete points.

Appendix D: Static magnetometry and ferromagnetic resonance measurements

Field hysteresis measurements of single magnetic layers of the control samples provided the saturation magnetization for each magnetic layer: $4\pi m_{Py} = 0.89{\cdot}10^7$ A/m and $4\pi m_{Pmd} = 2.25{\cdot}10^7$ A/m. Magnetization curves for a selected number of samples with t_{Ru} = 7, 12, 170 Å are shown as insets in Fig. 2 (f), (e) and (d) respectively. The $t_{Ru} = 7$ Å sample shows the behavior typical for a 90° coupling between Py and Pmd layers. A Ru thickness of $t_{Ru} = 12$ Å favors ferromagnetic (FM) coupling between magnetic layers and for a thick Ru spacer ($t_{Ru} = 170$ Å) the magnetic layers are de-coupled. Magnetometry results correlate well with the ferromagnetic resonance (FMR) measurements.

We measured the in-plane uniaxial anisotropy constants with angular dependent X-band (9.8 GHz) FMR (rotation about the surface normal) while the interlayer exchange constants (A_{ex} and B_{ex}) were determined from in-plane FMR measurements at varying excitation frequencies (2 - 12 GHz).The uniaxial anisotropy field is in-plane, i.e., it lies in the x-y plane. Here θ_i is the angle between the uniaxial easy axis and the magnetization at layer i. Then, the dependence of the uniaxial anisotropy field on θ_i angle is $(\boldsymbol{m}_i \cdot \widehat{\boldsymbol{e}}_u)\,\widehat{\boldsymbol{e}}_u = (m_i^x \cos\theta_i + m_i^y \sin\theta_i)\,(\cos\theta_i, \sin\theta_i, 0)$. In the samples considered here, the uniaxial anisotropy is along the x axis, i. e. $\theta_i = 0$. The angular dependent X-band measurements indicate that all samples exhibit a weak uniaxial anisotropy, with the largest anisotropy constant at about $K^u_{Pmd} = 2408\ J/m^3$ for Pmd and $K^u_{Py} = 184\ J/m^3$ for Py. Cubic anisotropy was found to be negligibly small: $K^c_{Pmd} = 179\ J/m^3$ and $K^c_{Py} = 10.6\ J/m^3$. Note that we consider the anisotropy constants as independent of the spacer layer thickness. All measured parameters are summarized in Table IV.

We determined A_{ex} and B_{ex} from fits of the resonant field vs. frequency as outlined in Ref. [54]. The sample with the thickest NM spacer layer ($t_{Ru} = 170$ Å) does not present any bilinear or biquadratic coupling, consistent with the M vs. H loops which show the switching of the individual layers (See inset in Fig. 2 (d)). As the Ru thickness decreases, interlayer-exchange coupling begins to correlate the switching of the two layers. The $t_{Ru} = 12$ Å sample shows FM coupling between magnetic layers with only a bilinear type of coupling present $A_{ex} = 4.5 \cdot 10^{-5}\,\mathrm{J/m^2}$; the field hysteresis loops confirm this as only a single switching field is evident (See inset in Fig. 2 (e)). Finally, for the $t_{Ru} = 7$ Å sample we find the bilinear exchange coupling constant $A_{ex} = 0$, although there is a large biquadratic coupling parameter $B_{ex} = -10.5 \cdot 10^{-5}\,\mathrm{J/m^2}$. This indicates that the coupling of the two layers is shifting from FM to AFM, leaving a ∼90° coupling between the Py and Pmd layers. Exchange constants together with the intrinsic dampings are summarized in Table II.

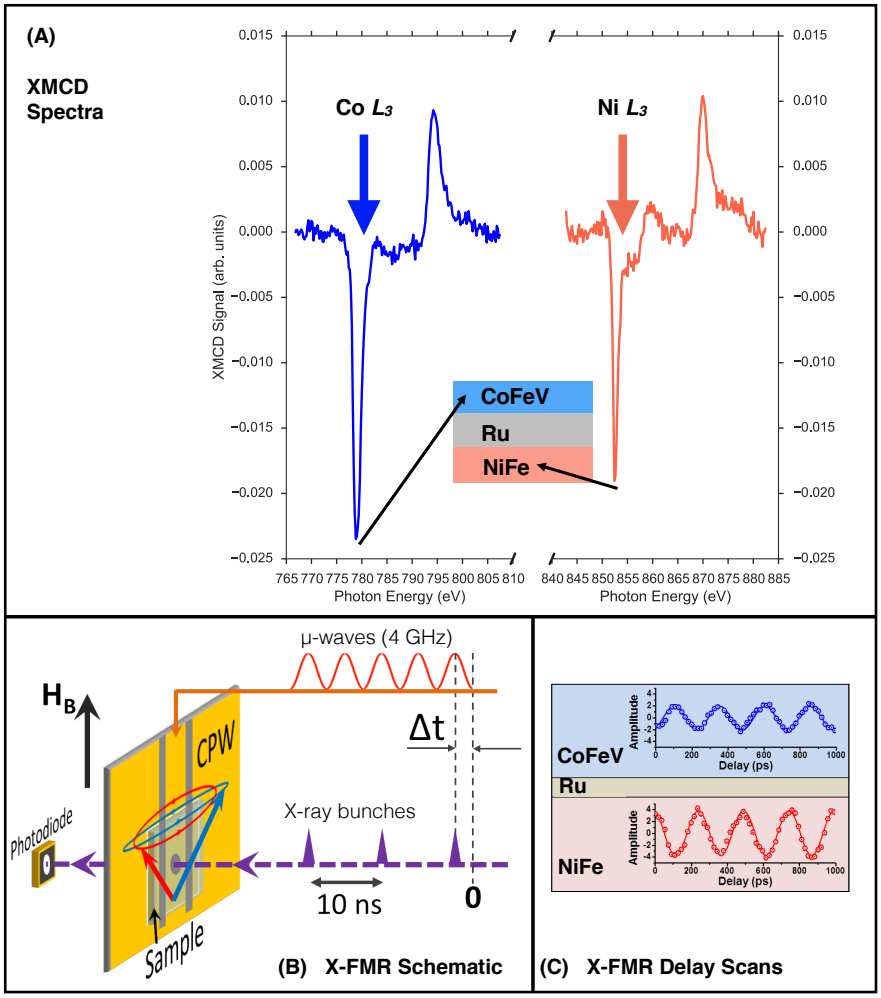

FIG. 5. (Color online) X-FMR principle and set-up. (a) XMCD spectra from a Pmd / Ru / Py trilayer. By tuning the photon energy to the Co (Ni) L_3 edge, the magnetization dynamics of the Pmd (Py) layer can be isolated from the collective response. (b) X-FMR scans are conducted in x-ray transmission mode. The sample is placed on a co-planar waveguide and the microwave excitation is synchronized with the x-ray bunches. A digital delay generator (not shown) varies the phase between the x-ray bunches and the *rf* excitation. (c) Typical delay scans from the Pmd or Py layer are sinusoidal functions, from which the amplitude and relative phase can be extracted.

TABLE IV. Measured physical magnitudes for Permalloy (Py) and Permendur (Pmd) layers.

Layer	K_i^u (J/m^3)	K_i^c (J/m^3)	d_i (m)	m_i^x (A/m)	ω (GHz)
Py ($i = 1$)	184.142	10.624	$8 \cdot 10^{-9}$	$(0.89 \cdot 10^7)/(4\pi)$	3.96
Pmd ($i = 2$)	2408.213	179.049	$8 \cdot 10^{-9}$	$(2.25 \cdot 10^7)/(4\pi)$	3.96

[1] K. Uchida, S. Takahashi, K. Harii, J. Ieda, W. Koshibae, K. Ando, S. Maekawa, and E. Saitoh, Nature **455**, 778 (2008).

[2] J. E. Hirsch, Physical Review Letters **83**, 1834 (1999).

[3] C.-F. Pai, L. Liu, Y. Li, H. W. Tseng, D. C. Ralph, and R. A. Buhrman, Applied Physics Letters **101**, 122404 (2012).

[4] N. Okuma, M. R. Masir, and A. H. MacDonald, Physical Review B **95**, 165418 (2017).

[5] L. J. Cornelissen, J. Liu, R. A. Duine, J. B. Youssef, and B. J. van Wees, Nature Physics **11**, 1022 (2015).

[6] B. L. Giles, Z. Yang, J. S. Jamison, and R. C. Myers, Physical Review B **92**, 224415 (2015).

[7] W. Yuan, Q. Zhu, T. Su, Y. Yao, W. Xing, Y. Chen, Y. Ma, X. Lin, J. Shi, R. Shindou, X. C. Xie, and W. Han, Science Advances **4**, eaat1098 (2018).

[8] J. C. Slonczewski, Journal of Magnetism and Magnetic Materials **159**, L1 (1996).

[9] L. Berger, Physical Review B **54**, 9353 (1996).

[10] T. Chen, R. K. Dumas, A. Eklund, P. K. Muduli, A. Houshang, A. A. Awad, P. Durrenfeld, B. G. Malm, A. Rusu, and J. Åkerman, Proceedings of the IEEE **104**, 1919 (2016).

[11] F. Hellman, A. Hoffmann, Y. Tserkovnyak, G. S. Beach, E. E. Fullerton, C. Leighton, A. H. MacDonald, D. C. Ralph, D. A. Arena, H. A. Dürr, P. Fischer, J. Grollier, J. P. Heremans, T. Jungwirth, A. V. Kimel, B. Koopmans, I. N. Krivorotov, S. J. May, A. K. Petford-Long, J. M. Rondinelli, N. Samarth, I. K. Schuller, A. N. Slavin, M. D. Stiles, O. Tchernyshyov, A. Thiaville, and B. L. Zink, Reviews of Modern Physics **89**, 025006 (2017).

[12] Y. Tserkovnyak, A. Brataas, and G. E. W. Bauer, Physical Review B **66**, 224403 (2002).

[13] M. R. Sears and W. M. Saslow, Physical Review B **85**, 014404 (2012).

[14] E. Saitoh, M. Ueda, H. Miyajima, and G. Tatara, Applied Physics Letters **88**, 182509 (2006).

[15] S. Mizukami, Y. Ando, and T. Miyazaki, Journal of Magnetism and Magnetic Materials **239**, 42 (2002).

[16] B. Heinrich, G. Woltersdorf, R. Urban, and E. Simanek, Journal of Applied Physics **93**, 7545 (2003).

[17] Y. Tserkovnyak, A. Brataas, and G. E. W. Bauer, Physical Review Letters **88**, 117601 (2002).

[18] B. Heinrich, Y. Tserkovnyak, G. Woltersdorf, A. Brataas, R. Urban, and G. E. W. Bauer, Physical Review Letters **90**, 187601 (2003).

[19] H. Yang, Y. Li, and W. E. Bailey, Applied Physics Letters **108**, 242404 (2016).

[20] M. Wang, W. Cai, K. Cao, J. Zhou, J. Wrona, S. Peng, H. Yang, J. Wei, W. Kang, Y. Zhang, J. Langer, B. Ocker, A. Fert, and W. Zhao, Nature Communications **9**, 671 (2018).

[21] S. Okamoto, N. Kikuchi, M. Furuta, O. Kitakami, and T. Shimatsu, Journal of Physics D: Applied Physics **48**, 353001 (2015).

[22] A. M. Deac, A. Fukushima, H. Kubota, H. Maehara, Y. Suzuki, S. Yuasa, Y. Nagamine, K. Tsunekawa, D. D. Djayaprawira, and N. Watanabe, Nature Physics **4**, 803 (2008).

[23] S. M. Mohseni, S. R. Sani, J. Persson, T. N. A. Nguyen, S. Chung, Y. Pogoryelov, P. K. Muduli, E. Iacocca, A. Eklund, R. K. Dumas, S. Bonetti, A. Deac, M. A. Hoefer, and J. Akerman, Science **339**, 1295 (2013).

[24] S. Sani, J. Persson, S. Mohseni, Y. Pogoryelov, P. Muduli, A. Eklund, G. Malm, M. Käll, A. Dmitriev, and J. Åkerman, Nature Communications **4**, 2731 (2013).

[25] I. McFadyen, E. Fullerton, and M. Carey, MRS Bulletin **31**, 379 (2006).

[26] E. Tsymbal, Journal of Magnetism and Magnetic Materials **130**, L6 (1994).

[27] Notice that in Eqs. (4)-(5) the sub-indexes of the susceptibility refer to its matrix elements.

[28] W. E. Bailey, L. Cheng, D. J. Keavney, C.-C. Kao, E. Vescovo, and D. A. Arena, Physical Review B **70**, 172403 (2004).

[29] T. Martin, G. Woltersdorf, C. Stamm, H. A. Durr, R. Mattheis, C. H. Back, and G. Bayreuther, Journal of Applied Physics **105**, 07D310 (2009).

[30] M. K. Marcham, P. S. Keatley, A. Neudert, R. J. Hicken, S. A. Cavill, L. R. Shelford, G. van der Laan, N. D. Telling, J. R. Childress, J. A. Katine, P. Shafer, and E. Arenholz, Journal of Applied Physics **109**, 07D353 (2011).

[31] P. Warnicke, R. Knut, E. Wahlstrm, O. Karis, W. E. Bailey and D. A. Arena, Journal of Applied Physics **113**, 033904 (2013).

[32] D. A. Arena, Y. Ding, E. Vescovo, S. Zohar, Y. Guan, and W. E. Bailey, Review of Scientific Instruments **80**, 083903 (2009).

[33] D. A. Arena, E. Vescovo, C.-C. Kao, Y. Guan, and W. E. Bailey, Physical Review B **74**, 064409 (2006).

[34] Y. Guan, W. E. Bailey, C.-C. Kao, E. Vescovo, and D. A. Arena, Journal of Applied Physics **99**, 08J305 (2006).

[35] W. E. Bailey, C. Cheng, R. Knut, O. Karis, S. Auffret, S. Zohar, D. Keavney, P. Warnicke, J.-S. Lee, and D. A. Arena, Nature Communications **4**, 2025 (2013).

[36] P. Warnicke, E. Stavitski, J.-S. Lee, A. Yang, Z. Chen, X. Zuo, S. Zohar, W. E. Bailey, V. G. Harris, and D. A. Arena, Physical Review B **92**, 104402 (2015).

[37] J. Li, L. R. Shelford, P. Shafer, A. Tan, J. X. Deng, P. S. Keatley, C. Hwang, E. Arenholz, G. van der Laan, R. J. Hicken, and Z. Q. Qiu, Physical Review Letters **117**, 076602 (2016).

[38] A. A. Baker, A. I. Figueroa, L. J. Collins-McIntyre, G. van der Laan, and T. Hesjedal, Scientific Reports **5**, 7907 (2015).

[39] A. Figueroa, A. Baker, L. Collins-McIntyre, T. Hesjedal, and G. van der Laan, Journal of Magnetism and Magnetic Materials **400**, 178 (2016).

[40] S. Parkin, Physical Review Letters **67**, 3598 (1991).

[41] Carl de Boor A Practical Guide to Splines. Springer-Verlag (1978).

[42] C. J. Durrant, L. R. Shelford, R. A. J. Valkass, R. J. Hicken, A. I. Figueroa, A. A. Baker, G. van der Laan, L. B. Duffy, P. Shafer, C. Klewe, E. Arenholz, S. A. Cavill, J. R. Childress, and J. A. Katine, Physical Review B **96**, 144421 (2017).

[43] N. Behera, M. S. Singh, S. Chaudhary, D. K. Pandya and P. K. Muduli, Journal of Applied Physics **17**, 17A714 (2015).

[44] M. Zwierzycki, Y. Tserkovnyak, P. J. Kelly, A. Brataas, and G. E. W. Bauer, Physical Review B **71**, 064420 (2005).

[45] K. Xia, P. J. Kelly, G. E. W. Bauer, A. Brataas, and

I. Turek, Physical Review B **65**, 220401 (2002).
[46] Y. Liu, Z. Yuan, R. Wesselink, A. A. Starikov, and P. J. Kelly, Physical Review Letters **113**, 207202 (2014).
[47] K. Carva and I. Turek, Physical Review B **76**, 104409 (2007).
[48] J. Chen, T. Yu, C. Liu, T. Liu, M. Madami, K. Shen, J. Zhang, S. Tu, M. S. Alam, K. Xia, M. Wu, G. Gubbiotti, Y. M. Blanter, G. E. W. Bauer, and H. Yu, Physical Review B **100**, 104427 (2019).
[49] P. Dürrenfeld, F. Gerhard, J. Chico, R. K. Dumas, M. Ranjbar, A. Bergman, L. Bergqvist, A. Delin, C. Gould, L. W. Molenkamp, and J. Åkerman, Physical Review B **92**, 214424 (2015).
[50] N. Roschewsky, T. Matsumura, S. Cheema, F. Hellman, T. Kato, S. Iwata, and S. Salahuddin, Applied Physics Letters **109**, 112403 (2016).
[51] W. Zhang, W. Han, X. Jiang, S.-H. Yang, and S. S. P. Parkin, Nature Physics **11**, 496 (2015).
[52] S. Takahashi, Applied Physics Letters **104**, 052407 (2014).
[53] T. Chiba, G. E. W. Bauer, and S. Takahashi, Physical Review B **92**, 054407 (2015).
[54] Y. Wei, S. Jana, R. Brucas, Y. Pogoryelov, M. Ranjbar, R. K. Dumas, P. Warnicke, J. Akerman, D. A. Arena, O. Karis and P. Svedlindh. Journal of Applied Physics **115**, 17D129 (2014).
[55] A. A. Baker, A. I. Figueroa, C. J. Love, S. A. Cavill, T. Hesjedal and G. Van Der Laan, Physical Review Letters **116**, 1 (2016).
[56] A. A. Baker, A. I. Figueroa, D. Pingstone, V. K. Lazarov, G. Van Der Laan and T. Hesjedal, Scientific Reports **6**, 1 (2016).